Metasurface enhanced sensitized photon upconversion: towards highly efficient low power upconversion applications and nano-scale E-field sensors

Christian Würth[1*], Phillip Manley[2,3], Robert Voigt[1], Doğuşcan Ahiboz[2], Christiane Becker[2*], Ute Resch-Genger[1]

[1] Federal Institute for Materials Research and Testing (BAM), Biophotonics, Richard-Willstaetter-Str. 11, 12489 Berlin, Germany
[2] Helmholtz-Zentrum Berlin für Materialien und Energie GmbH, Albert-Einstein-Str. 16, 12489 Berlin, Germany
[3] Zuse Institute Berlin, Takustraße 7, 14195 Berlin, Germany

KEYWORDS: Upconversion, nanoparticles, photonic crystals, metasurface, field sensor, emission enhancement

ABSTRACT

Large scale nanoimprinted metasurfaces based on silicon photonic crystal slabs were produced and coated with a $NaYF_4$:Yb^{3+}/Er^{3+} upconversion nanoparticle (UCNP) layer. UCNPs on these metasurfaces yield a more than 500-fold enhanced upconversion emission compared to UCNPs on planar surfaces. It is also demonstrated how the optical response of the UCNPs can be used to estimate the local field energy in the coating layer. Optical simulations using the finite element method validate the experimental results and the calculated spatial three-dimensional field energy distribution helps to understand the emission enhancement mechanism of the UCNPs closely attached to the metasurface. In addition, we analyzed the spectral shifts of the resonances for uncoated and coated metasurfaces and metasurfaces submerged in water to enable a prediction of the optimum layer thicknesses for different excitation wavelengths paving the way to applications such as electromagnetic field sensors or bioassays.

TOC

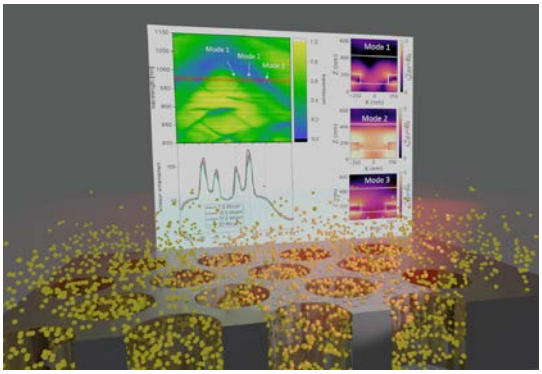

A recently emerged class of nanoscale reporters are lanthanide-based upconversion nanoparticles (UCNPs),[1-3] that have been intensively studied in the material[4-8] and life sciences[9-16] because of their potential to convert light between different spectral regions and their unique photophysical properties. UCNPs show several sharp emission bands, an exceptionally high photostability,do not blink, and enable autofluorescence free sensing and imaging applications. One major drawback of the nonlinear population dynamics are low luminescence quantum yields which strongly depend on the number of photons absorbed per time interval and thus on excitation power density.
To enhance the upconversion efficiency of UCNPs several approaches were studied. UCNP architecture was optimized using different shelling procedures and arrangements.[17-19], and doping concentration.[20, 21] Also, the host materials were varied to enhance energy transfer rates between lanthanide ions and

reduce surface quenching which is the major quenching channel.[22, 23] Other approaches focused on strategies to locally enhance the electromagnetic field energy[24] using as lensing[25, 26], plasmon resonances[27-32], opal-like photonic crystals[33, 34] and photonic crystal slabs[35-38] or combinations of these effects[38, 39]. Some of these field enhancement strategies were limited to small areas because of challenging synthesis and manufacturing steps. Metasurfaces or photonic crystal slabs can be produced in large dimensions and with high throughput. Recent concepts to combine UCNPs and photonic crystals used holographic or electron beam approaches for dielectric PhC production,[35, 38] employing silicon nano pillars[35] and UCNP filled hole arrays[38] based on Si_3N_4. This yielded already upconversion emission enhancements of 400 or 350 fold, respectively. Silicon processing is a well-established technology, which enables to use state-of-the-art production methods to reach application-relevant substrate dimensions of several centimeters. Particularly, the nanoimprinting technology offers large scale, low cost, and high throughput production of structured rigid and flexible silicon substrates.[40-43]

Here we focused on the preparation, optimization and understanding of silicon metasurfaces produced by nanoimprint technology to enhance the sensitized upconversion efficiency of Yb^{3+}/Er^{3+} co-doped $NaYF_4$ nanoparticles. We deliberately used UCNPs that can be easily produced in large amounts via a one batch synthesis[44] as well as core-shell particles. $NaYF_4$:Yb^{3+}/Er^{3+} particles are currently the most studied UCNPs. We demonstrate that although the photon energy typically used to excite Yb^{3+} of 1.27 eV (976 nm) is larger than the indirect silicon bandgap, strong upconversion enhancements of 1000 can be realized for spin coated PMMA/UCNP thin films. The resonance of the presented structures can be tuned by adjusting metasurface thickness[45, 46] and tuned to other spectral positions. Additionally, we find a good agreement between optical simulations and experimental data. This allows to predict enhancement factors and, alternatively, UCNP use as a nanoscale electric field energy sensor.

Figure 1a) illustrates the energy scheme of Yb^{3+}/Er^{3+} co-doped UCNPs including typical transitions, the corresponding emission wavelengths, and colors. To study the near-surface electric field enhancement and emission enhancement of UCNPs near the metasurface, $NaYF_4$ core only and core-shell oleate stabilized UCNPs of roughly 25 nm were synthesized (see SI) that are colloidally stable, monodisperse, dispersible in various organic solvents, and can be easily embedded into polymers as prerequisite for homogeneous high-quality coatings. A typical doping concentration of 20% Yb^{3+}/2% Er^{3+} was chosen (see Figure 1b).[44] Particle characterization using transmission electron microscopy (TEM) images, particle size distributions, excitation power dependent quantum yields and red to green intensity ratios are shown in Figure 1. Depending on the excitation power density (*P*) the red emission band ($^4F_{9/2}$) of Er^{3+} can be either populated via a two or three photon process, its contribution to the overall emission is therefore strongly *P*-dependent (see Figure 1 c) and d).[23, 47] This relative contribution of the red emission band to the overall emission I_{red}^{rel} can be used to correlate the emission characteristics of UCNPs with the corresponding local *P* or electric field energy. For emission enhancement studies PMMA/UCNP films were spin coated with thicknesses between 100-250 nm. Due to the small layer thickness the direct characterization such as quantum yield and *P*-dependent measurements of the emission spectra with the integrating sphere setup used for particle characterization is challenging. To correlate $I_{red}^{rel}(P)$ special care must be taken because surface near organic molecule vibrations influence the UCNP optical properties by bridging energy gaps between lanthanide energy levels and quench the emission.[23, 48] To characterize the basic optical properties of the UCNPs in an environment similar to the spin coated films, the UCNPs were transferred to cyclohexane, chloroform and incorporated into PLMA layers after the synthesis and the *P*-dependent emission characteristics and quantum yields were investigated Figure 1c)-e). In addition to steady state spectroscopy lifetime measurements were done to compare the optical properties of the UCNPs in PMMA, PLMA, and liquids (see Figure f)). This comparison shows identical decay characteristics of the UCNPs in spin coated PMMA layers with thicknesses of some 100 nm and PLMA of several mm and a mismatch to UCNPs in e.g. chloroform. Therefore, the population dynamics that cause the different red to green intensity

ratios are similar for the PLMA and PMMA environment. PLMA has the big advantage over PMMA that it is flexible and can be geometrically easily adapted to different experimental requirements. The fit of the contribution of the red emission band of UCNPs embedded in a PLMA Figure 1d) was further used to estimate the *P* enhancement of the metasurface resonances.

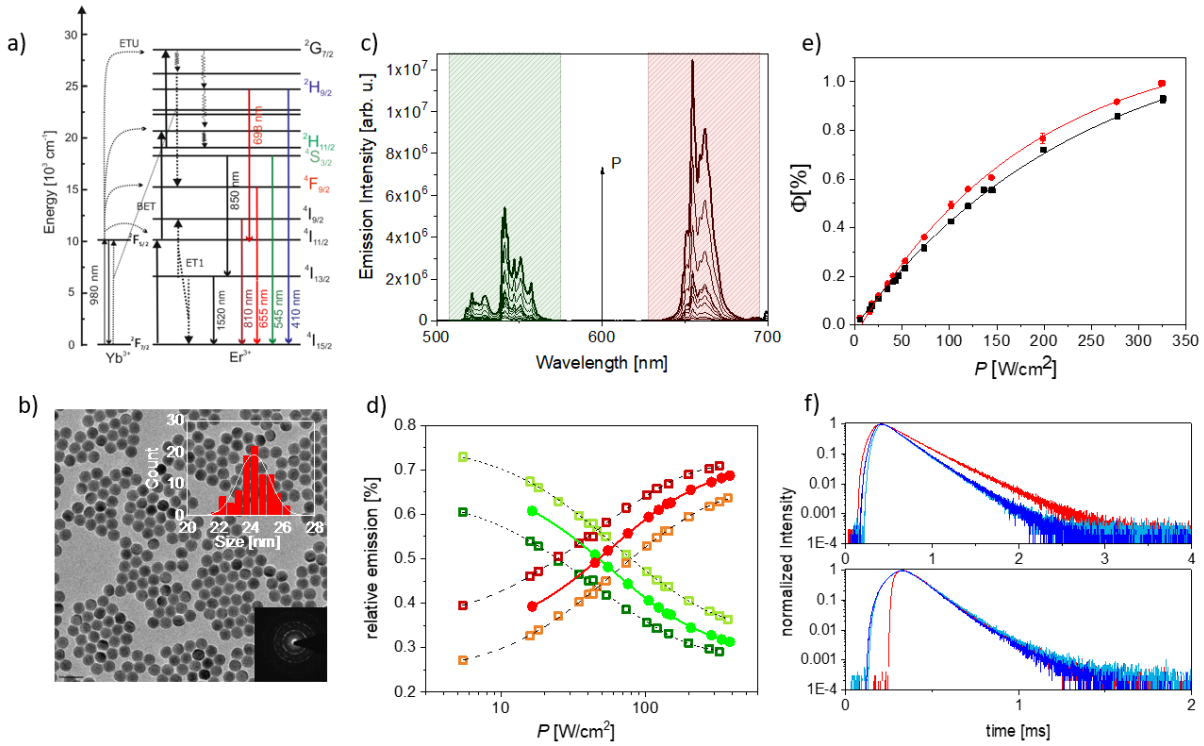

Figure 1: a) Energy scheme of Yb^{3+}/Er^{3+} co-doped UCNPs, b) representative TEM image and particle size distribution of the used core only particles, c) emission spectra of UCNPs embedded in PLMA for excitation powers between 16 and 380 W/cm² d) *P* dependent relative contribution of the red I_{red}^{rel} and green I_{green}^{rel} emission band for core only UCNPs in PLMA (red and green circles), chloroform (dark red and dark green open squares) and cyclohexane (light redand light green open squares). e) excitation power dependent quantum yields of core only UCNPs in cyclohexane (black) and chloroform (red), f) represents the decay kinetics of the red (upper panel) and green (lower panel) emission band of core-only particles in chloroform (red), PMMA (light blue) and PLMA (dark blue).

The metasurfaces were prepared by physical vapor deposition of silicon with defined thickness on glass substrates with a nanoimprinted surface structure and subsequent etching and abrasion steps (see SI). This yielded hexagonal hole arrays with a lattice constant of *d* = 600 nm and a hole diameter of 325 nm (Figure 2 a) and b)). A sufficiently large area of the silicon coating was left unstructured and used as reference region to quantify the emission enhancement in the metasurface regions (see Figure 2a). The PMMA/UCNP layer was spin coated on top of the structured and the planar silicon region Figure 2c). Special care was taken to ensure a homogeneous coating of both substrate regions. SEM and AFM measurements demonstrate the homogeneous coating with a thickness of roughly 200 nm and nearly closed packed UCNPs. To identify the spectral and angular positions of the metasurface resonances, transmittance measurements were performed. Figure 2 d) and e) show angularly resolved transmittance measurements of an uncoated and an UCNP/PMMA coated metasurface. The resonances indicate the spectral position of the leaky modes which are often accompanied by strongly enhanced near-fields. The refractive index change from 1.0 for air to 1.48 for PMMA shifts the resonances approximately 50 nm to longer wavelengths, which must be considered for further metasurface design. To tackle bioanalytical applications like assays or sensor arrays the induced mode shift by water (*n*=1.33) for the same metasurface was also investigated. Contrary to the thin spin coated UCNP/PMMA layer of only 200 nm the metasurface was immersed into a water bath for these

measurements. The resulting red shift of the leaky metasurface modes is comparable to that induced by the relatively thin UCNP/PMMA layer (Figure 2f).

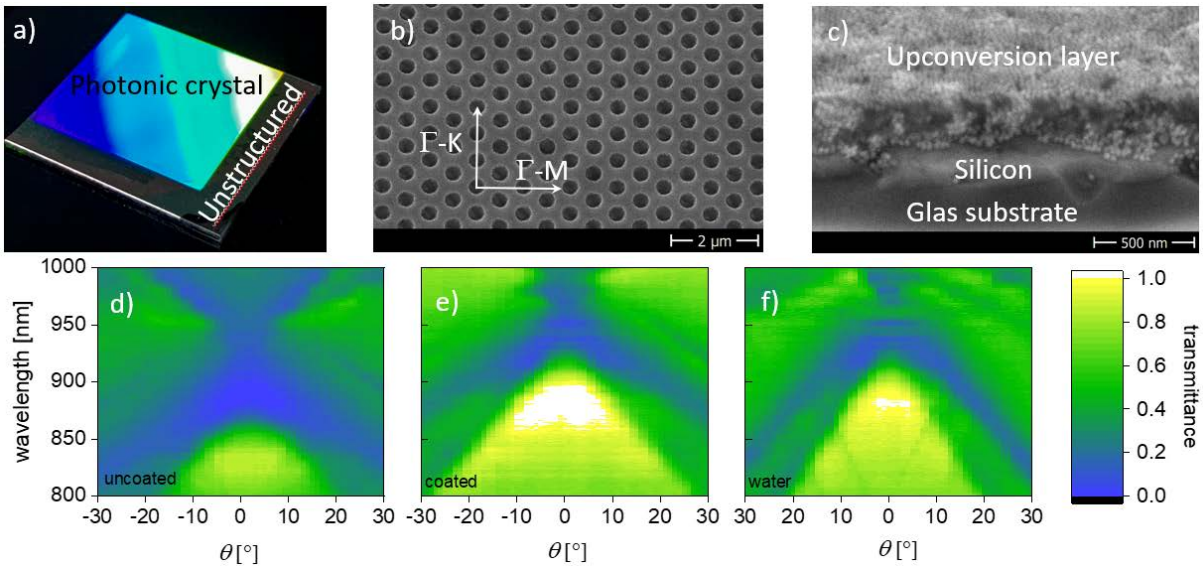

Figure 2: a) Photo of a silicon metasurface on glass substrate (shiny part) with unstructured reference region (edges), b) SEM image of the metasurface with indicated high-symmetry directions. c) SEM image of a PMMA/UCNP coated metasurface. d)-e) Angularly and spectrally resolved transmitance maps of d) the uncoated metasurface, e) PMMA/UCNP coated metasurface and f) the uncoated metasurface submerged in water.

To further predict spectral resonance positions and an optimized design, calculations using the finite element method were performed that consider the geometry and refractive indices of the silicon, coating and substrate (see SI). Comparisons of transmittance measurements and calculations are shown in Figure 3a) and S5. The simulations excellently agree with the experimental data, butalso indicate that the experimental data contain contributions from different polarizations. Contributions of transverse electric (TE) modes in the experimental transverse magnetic (TM) arrangement and vice versa are observed. This could be caused by small sample miss-alignments in the experimental setup or by a misorientation of the metasurface with respect to the edges of the macroscopic substrate.

To quantify the emission enhancement resulting from the interaction of the metasurface resonances with the UCNP layer, angularly resolved emission measurements were performed for the metasurface rotated along the high symmetry directions Γ-K and Γ-M (see also Figure 2a,b) and for the different polarizations (TE and TM) of the excitation laser. The custom-made experimental setup used is detailed in the SI. Special care was taken to spectrally correct the setup´s detection channel to ensure comparable red to green intensity ratios as obtained with other spectrometers. The emission enhancement is calculated as the ratio of the overall upconversion emission intensity under 976 nm excitation in the spatial areas of the structured metasurface region and the unstructured reference region. Figure 3 c) and d) show the emission enhancement for a 50 nm thick silicon metasurface with a 200 nm UCNP/PMMA coating for rotation along the Γ-M and Γ-K direction, respectively, as function of the angle of incidence (θ) of the 976 nm TM-polarized laser. The spectral positions of the metasurface resonances are indicated in the transmittance spectra below. The bandwidth of the excitation laser is highlighted as a red band. The UC emission enhancement is particulary large when the laser wavelength overlaps with metasurface resonances. Then, emission enhancement factors of up to 300 were observed for low P (7.5 W/cm^2). The occasionally observed small deviations between transmittance and UC emission measurements are ascribed to discrepancies in the spot positions of the experimental setups on the metasurface.

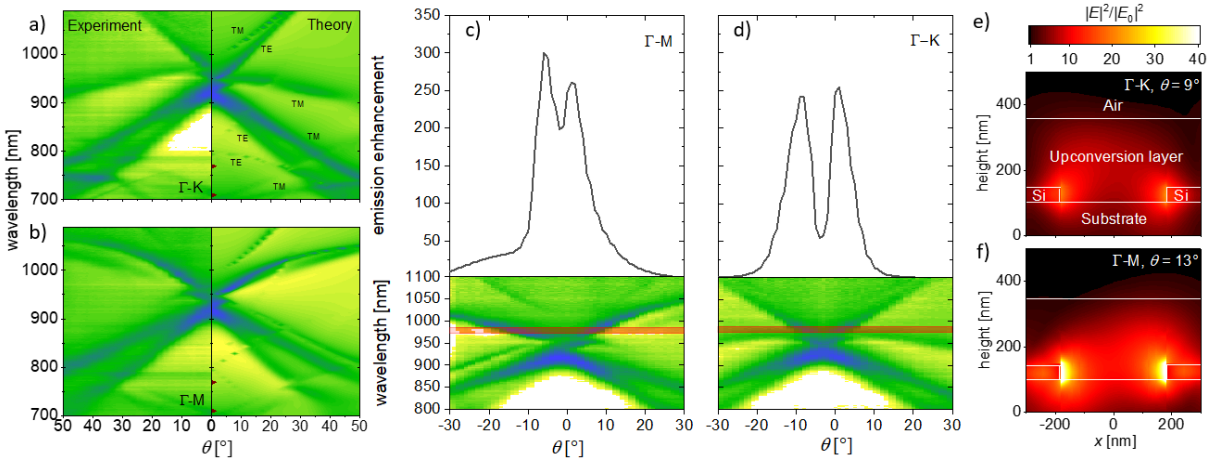

Figure 3: a) & b) Comparison of measured (left) and simulated (right) transmittance of averaged TE and TM polarized light through the metasurface coated with 200 nm UCNP/PMMA when rotated in Γ-K (a)) and Γ-M (b)) direction (silicon thickness: 50 nm, coating thickness: 200 nm). c) & d) Measured enhancement factor of the UC emission (upper part) as function of the incident angle (θ) at an excitation power density of 7.5 W/cm² for TM polarized light and rotation in Γ-M (c)) and Γ-K (d)) direction; corresponding measured transmittance maps are shown in the lower part with the excitation wavelength indicated by a red band. See Figure 2 for transmittance colour map of all four transmitance maps shown here. e) and f) corresponding spatially resolved electric field distribution.

For future applications in the life and material sciences an emission enhancement at normal incidence (i.e. 0°) is often desired. Small changes in metasurface thickness already shift the spectral positions of the resonances making a perfect experimental adjustment of the mode positions matching 976 nm challenging. Furthermore, for some metasurface resonances the coupling of external radiation at normal incidence is suppressed if they form a symmetry-protected bound state in continuum.[49, 50] In Figure 3 the 0° resonance is not perfectly located at 976 nm but still an emission enhancement factor of up to 200 was obtained at normal incidence. At near normal incidence where a resonance perfectly matches the excitation conditions, enhancement factors of up to 300 can be realized. This underlines the potential of our approach. Simulations of the electric field energy ($|E^2|$) shown in Figure 3 e) and f) indicate strong hot spots near the vertical planes and inside the holes for the respective resonances. A more detailed analysis of the spatial distribution of enhancements for TE and TM modes is shown in Figure S8.

To optimize the overlap of the resonance mode volume and the UCNP layer, as well as the absolute near field enhancement value, we varied the thickness of the silicon and the UCNP layer. Therefore, a 120 nm thick metasurfaces was produced and coated with different thicknesses of the upconversion layer. Compared to the 50 nm Si-layer shown in Fig. 2 and 3 the resonances are shifted to longer wavelengths due to the increased PhC thickness.[45, 46] The UCNP/PMMA coating thicknesses were determined by AFM to be approximately 120 nm and 220 nm (see Figure S9 to S11) and used for subsequent calculations. Coatings with thicknesses near 200 nm form a flat surface on top of the underlying metasurface in contrast to thinner coatings near 100 nm. For the latter, the holes of the metasurface structures were filled but the surface morphology still follows the metasurface in a conformal manner, meaning that the indentation of metasurface hole was still visible. In both cases the UCNPs form a nearly closed packed particle layer filling the layer volume (Figure S11). Figure 4 summarizes the experimental and theoretical results for the uniform coating. Figure 4 a) and b) illustrate the excellent correlation between the experimentally determined emission enhancement and the spectral position of the metasurface resonances. Contrary to the 50 nm thick silicon structures the 120 nm thick metasurface shows additional narrow modes at 976 nm at $\theta = 9°$ and $\theta = 17°$. These narrow modes (mode 1 and 2) lead to a considerably higher emission enhancement than the spectrally broadened modes located at 976 nm at an angle of approximately 30° (mode 3). Calculation of the E-

field distribution inside the coating layer for modes 1 to 3 confirm the stronger local $|E^2|$ for narrow modes with higher quality factors (Figure 4f). The calculated volume integrated *E*-field energy enhancement was therefore correlated with the effective experimentally determined emission enhancement. Figure 4c shows the angularly resolved relative spectral contribution of the red and green emission bands of Er^{3+} to the overall upconverted emission intensity. The amount of the red emission, which increases with *P* because of its increasing three photonic character (see also Figure 1), can be used as a measure for the *P* enhancement or in this case as a measure of $|E^2|$ inside the coating layer. Figure 4d shows the determined *P* using the fits shown in Figure 1d as a correlation function for $I_{red}^{rel}(P)$ and in consequence $I_{red}^{rel}(|E^2|)$. The experimentally determined enhancement factors agree well with the theoretical predictions (see Figure 4e). Relative $|E^2|$ or *P* enhancements of up to 10 were reached. In contrast to the metasurfaces with roughly 50 nm silicon thickness the 120 nm thick metasurfaces show the localization of the electric field on the plateaus (see Figure 4f and S13).

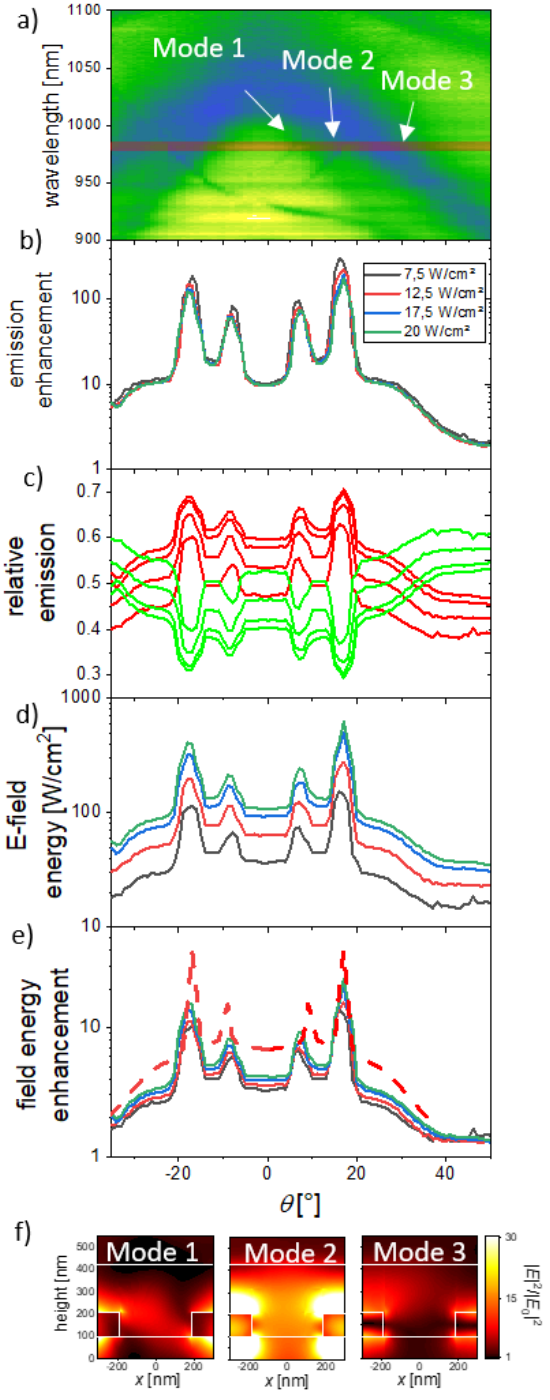

Figure 4: a) Angularly resolved transmittance measurement of a 110 nm metasurface with 200 nm UCNP/PMMA coating for identification of the spectral positions metasurface resonances with indicated laser wavelength (red, for transmitance colour map see Figure 2), b) measured angular resolved UC emission enhancement for different laser spot power densities (7.5 W/cm² (black), 12.5 W/cm² (red) 17.5 W/cm² (blue) and 20 W/cm² (green)), c) relative contributions of the red and green emission bands to the overall emission, d) calculated angular resolved excitation power densities, e) experimentally determined excitation power/field energy enhancement in comparison with theoretical predictions (broken red line), f) field energy distribution for the indicated modes 1 to 3.

For the thin coatings of roughly 125 nm a different UCNP/PMMA mixture was used. The UCNPs had a core shell structure with a thin shell of <1nm. Special care was taken that the optical properties are comparable to that of the core only particles discussed above (see SI Figure S5, S6). For the thin UCNP/PMMA layers even stronger emission enhancements were determined in comparison to the thick coatings. Emission enhancement factors of up to 1000 were achieved for the thin and > 100 for the thick coating layer (see Figure 4b, 5b).

Calculations confirm that the volume integrated $|E^2|$ enhancement is stronger for thin films and indicate that layer thickness plays a significant role for the local $|E^2|$. This, together with the influence of the spatially localized EM-fields, lead to smaller enhancement factors for thick coatings. Apparently, averaging over volume with low and high field energies reduces the enhacement factors. UCNPs close to the metasurface feel a much stronger E-field compared to UCNPs close to the coating/air interface. Close to the metasurface *E* field enhacement factors of about 100 can be realized. This implies that the correlation of the overall emission enhancement, quantum yield increase and emission colour of the UCNP coating has to be treated with care. The distribution of high $|E^2|$ regions is inhomogeneous inside the UCNP layer, therefore the emission spectra and integrated photon fluxes represent values averaged over the detection volume that are, however, dominated by the characteristics of the high $|E^2|$ regions due to the nonlinear optical response of the UCNP emission. For thin coatings (125 nm), the relative contribution of the red emission is even higher than for the 220 nm coatings and strongly exceeds the correlation shown in Figure 1, hampering the $|E^2|$ estimation but indicating $|E^2|$ > 400 W/cm².

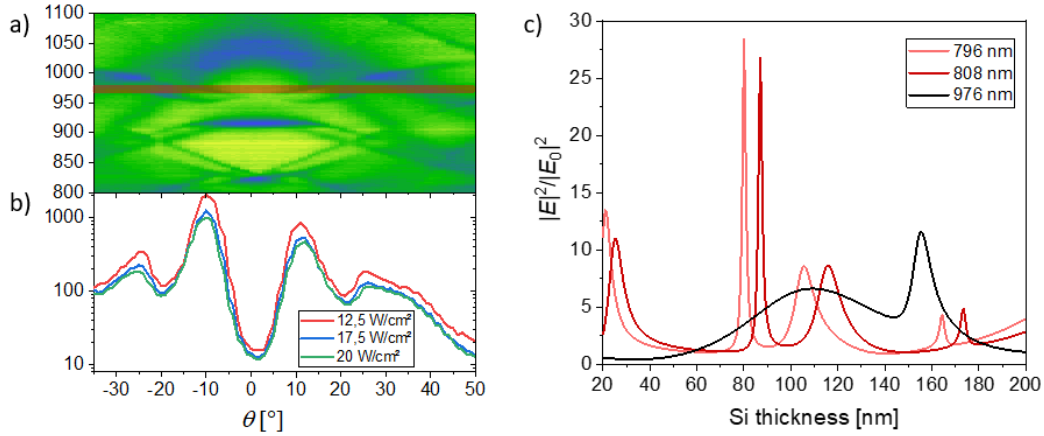

Figure 5: a) Angular resolved transmittance measurement in the Γ-K direction of a 125 nm metasurface with 125 nm UCNP/PMMA coating for identification of the spectral positions metasurface resonances with indicated laser wavelength (red, for transmitance colour map see Figure 2), b) Measured angular resolved UC emission enhancement c) Silicon metasurface thickness dependence of the volume averaged $|E^2|$ enhancement in water for excitation wavelength of 796 nm, 808 nm and 976 nm at θ = 0°.

For further geometrical optimizations, a theoretical approach is favorable to not only screen the mode positions and $|E^2|$ of the large amount of possible geometries of the metasurface, but also to predict the possible upconversion enhancement. For the particles used in this study already a quadratic approximation of the emission intensity dependence on the field energy gave reasonable results (Figure S15, S16).

The transmittance measurements as well as the corresponding calculations of the dispersion relation of the metasurfaces show resonances that can, with slight adjustment, also be used to enhance Nd^{3+} sensitized upconversion at excitation wavelength of 808 nm or preferably 796 nm[51] (see Figure 5, S12). For applications in aqueous media this excitation wavelength is preferred as it minimizes water absorption-related attenuation and heating effects.[51] Figure 5c summarizes the theoretical prediction of $|E^2|$ enhancement for typical wavelength used for Nd^{3+} and Yb^{3+} sensitized upconversion in dependence of the silicon metasurface thickness in an aqueous medium at θ = 0°.

In conclusion, we showed strong angularly resolved upconversion emission enhancements of >500 of Yb^{3+}, Er^{3+} doped lanthanide nanoparticles induced by surface near field energy enhancement effects on metasurfaces. We demonstrated that the red and green emission bands of Yb^{3+}/Er^{3+} doped UCNPs can be used as nanoscale field sensors to estimate the local field energy experimentally. The spatial distribution of the E-field energy inside the UCNP-layer was calculated to explain coating thickness dependent emission enhancement effects and the theoretically determined spectral positions of the leaky metasurface resonances considering the optical properties of the coating layer show excellent agreement with the experimental data. Leaky metasurface resonances can be shifted by adjustment of silicon thickness to match the sensitizer´s absorbance band and made predictions for optimum metasurface thicknesses for θ = 0°. Further our results indicate that oblique angles of incidence may cause narrow resonances with high quality factors and high E-field enhancements. To aim for applications the metasurfaces used in this study were produced by nanoimprint-lithography and thin-film technologies in application relevant dimensions of several square centimeters. This dimensions are sufficient for e.g. bioassays and the E-field distribution near the metasurface is in good agreement with expected binding distances of an upconversion reporter. These results can pave the road for the development of low cost and optimized low power upconversion applications with the potential of theoretical prescreening and UCNPs as E-field sensors. In perspective also other particle architectures and compositions as the ones used in this study can be employed for further optimized $|E^2|$ sensing and maximum emission enhancements. For sensing of strong $|E^2|$ small particles[22] or low doping concentrations[20, 52] should be beneficial to increase the dynamic range of the red emission contribution before reaching saturation of the $^4F_{9/2}$ and $^4S_{3/2}$ -levels. For low $|E^2|$ higher doping concentrations and bigger particles can be beneficial.[22, 53] To achieve maximum emission intensities, particles with high Er^{3+} content could help to overcome saturation at medium excitation power densities.[54] We assume that with the right choice of particle composition, size and architecture and metasurface geometry much higher enhancement factors than those presented in this study can be achieved.

ASSOCIATED CONTENT

Supporting Information: particle characterization, finite element theory, AFM characterization, calculation results, additional experimental data.

AUTHOR INFORMATION

Corresponding Author

Christian Würth, Email: christian.wuerth@bam.de, https://orcid.org/0000-0002-0204-9727
Christiane Becker, Email: christiane.becker@helmholtz-berlin.de, https://orcid.org/0000-0003-4658-4358

Author Contributions

CW measurements, design of setup and experiments, writing; PM: finite element calculations, RV: setup development and measurements, DA: PhC produced, CB: writing and PhC design, URG writing and organization. All authors reviewed the MS.

Funding Sources

PM thanks the Helmholtz Association for funding within the Helmholtz Excellence Network SOLARMATH a strategic collaboration of MATH+ and Helmholtz-Zentrum Berlin (grant no. ExNet-0042-Phase-2-3). URG gratefully acknowledges financial support from the German Research Council (DFG; grant RE 1203/20-1; M-EraNet program)

Notes

The authors declare no competing financial interest.

ACKNOWLEDGMENT

We thank S. Radunz (BAM) and the Group of T. Hirsch (University of Regensburg) for particle synthesis.

REFERENCES

1. Zhou, J.; Liu, Q.; Feng, W.; Sun, Y.; Li, F., Upconversion Luminescent Materials: Advances and Applications. *Chemical Reviews* **2015,** *115* (1), 395-465.
2. Gnach, A.; Bednarkiewicz, A., Lanthanide-doped up-converting nanoparticles: Merits and challenges. *Nano Today* **2012,** *7* (6), 532-563.
3. Zhou, B.; Shi, B.; Jin, D.; Liu, X., Controlling upconversion nanocrystals for emerging applications. *Nat Nano* **2015,** *10* (11), 924-936.
4. Wang, H. Q.; Batentschuk, M.; Osvet, A.; Pinna, L.; Brabec, C. J., Rare-Earth Ion Doped Up-Conversion Materials for Photovoltaic Applications. *Advanced Materials* **2011,** *23* (22-23), 2675-2680.
5. Goldschmidt, J. C.; Fischer, S., Upconversion for Photovoltaics - a Review of Materials, Devices and Concepts for Performance Enhancement. *Adv. Opt. Mater.* **2015,** *3* (4), 510-535.
6. Wang, F.; Liu, X. G., Recent advances in the chemistry of lanthanide-doped upconversion nanocrystals. *Chemical Society Reviews* **2009,** *38* (4), 976-989.
7. Shikha, S.; Salafi, T.; Cheng, J. T.; Zhang, Y., Versatile design and synthesis of nano-barcodes. *Chemical Society Reviews* **2017,** *46* (22), 7054-7093.
8. Zhou, J. J.; Leano, J. L.; Liu, Z. Y.; Jin, D. Y.; Wong, K. L.; Liu, R. S.; Bunzli, J. C. G., Impact of Lanthanide Nanomaterials on Photonic Devices and Smart Applications. *Small* **2018,** *14* (40), 29.
9. Shen, J.; Zhao, L.; Han, G., Lanthanide-doped upconverting luminescent nanoparticle platforms for optical imaging-guided drug delivery and therapy. *Adv. Drug Deliv. Rev.* **2013,** *65* (5), 744-755.
10. Wu, X.; Chen, G. Y.; Shen, J.; Li, Z. J.; Zhang, Y. W.; Han, G., Upconversion Nanoparticles: A Versatile Solution to Multiscale Biological Imaging. *Bioconjugate Chemistry* **2015,** *26* (2), 166-175.
11. Xu, C. T.; Zhan, Q. Q.; Liu, H. C.; Somesfalean, G.; Qian, J.; He, S. L.; Andersson-Engels, S., Upconverting nanoparticles for pre-clinical diffuse optical imaging, microscopy and sensing: Current trends and future challenges. *Laser & Photonics Reviews* **2013,** *7* (5), 663-697.
12. Zheng, W.; Huang, P.; Tu, D.; Ma, E.; Zhu, H.; Chen, X., Lanthanide-doped upconversion nano-bioprobes: electronic structures, optical properties, and biodetection. *Chemical Society Reviews* **2015**.
13. Chen, G. Y.; Qju, H. L.; Prasad, P. N.; Chen, X. Y., Upconversion Nanoparticles: Design, Nanochemistry, and Applications in Theranostics. *Chemical Reviews* **2014,** *114* (10), 5161-5214.
14. Gorris, H. H.; Wolfbeis, O. S., Photon-upconverting nanoparticles for optical encoding and multiplexing of cells, biomolecules, and microspheres. *Angew Chem Int Ed* **2013,** *52* (13), 3584-3600.
15. Escudero, A.; Becerro, A. I.; Carrillo-Carrion, C.; Nunez, N. O.; Zyuzin, M. V.; Laguna, M.; Gonzalez-Mancebo, D.; Ocana, M.; Parak, W. J., Rare earth based nanostructured materials: synthesis, functionalization, properties and bioimaging and biosensing applications. *Nanophotonics* **2017,** *6* (5), 881-921.

16. Zhang, Z. M.; Shikha, S.; Liu, J. L.; Zhang, J.; Mei, Q. S.; Zhang, Y., Upconversion Nanoprobes: Recent Advances in Sensing Applications. *Anal. Chem.* **2019,** *91* (1), 548-568.
17. Pilch, A.; Würth, C.; Kaiser, M.; Wawrzynczyk, D.; Kurnatowska, M.; Arabasz, S.; Prorok, K.; Samoc, M.; Strek, W.; Resch-Genger, U.; Bednarkiewicz, A., Shaping Luminescent Properties of Yb3+ and Ho3+ Co-Doped Upconverting Core-Shell beta-NaYF4 Nanoparticles by Dopant Distribution and Spacing. *Small* **2017,** *13* (47), 13.
18. Würth, C.; Fischer, S.; Grauel, B.; Alivisatos, A. P.; Resch-Genger, U., Quantum Yields, Surface Quenching, and Passivation Efficiency for Ultrasmall Core/Shell Upconverting Nanoparticles. *J. Am. Chem. Soc.* **2018,** *140* (14), 4922-4928.
19. Hudry, D.; Howard, I. A.; Popescu, R.; Gerthsen, D.; Richards, B. S., Structure-Property Relationships in Lanthanide-Doped Upconverting Nanocrystals: Recent Advances in Understanding Core-Shell Structures. *Advanced Materials* **2019,** *31* (26), 25.
20. Kaiser, M.; Würth, C.; Kraft, M.; Soukka, T.; Resch-Genger, U., Explaining the influence of dopant concentration and excitation power density on the luminescence and brightness of beta-NaYF4:Yb3+,Er3+ nanoparticles: Measurements and simulations. *Nano Res.* **2019,** *12* (8), 1871-1879.
21. Wen, S. H.; Zhou, J. J.; Zheng, K. Z.; Bednarkiewicz, A.; Liu, X. G.; Jin, D. Y., Advances in highly doped upconversion nanoparticles. *Nat. Commun.* **2018,** *9*, 12.
22. Kraft, M.; Würth, C.; Muhr, V.; Hirsch, T.; Resch-Genger, U., Particle-size-dependent upconversion luminescence of NaYF4: Yb, Er nanoparticles in organic solvents and water at different excitation power densities. *Nano Res.* **2018,** *11* (12), 6360-6374.
23. Würth, C.; Kaiser, M.; Wilhelm, S.; Grauel, B.; Hirsch, T.; Resch-Genger, U., Excitation power dependent population pathways and absolute quantum yields of upconversion nanoparticles in different solvents. *Nanoscale* **2017,** *9* (12), 4283-4294.
24. Xu, W.; Chen, X.; Song, H. W., Upconversion manipulation by local electromagnetic field. *Nano Today* **2017,** *17*, 54-78.
25. Liang, L. L.; Teh, D. B. L.; Dinh; Chen, W. D.; Chen, Q. S.; Wu, Y. M.; Chowdhury, S.; Yamanaka, A.; Sum, T. C.; Chen, C. H.; Thakor, N. V.; All, A. H.; Liu, X. G., Upconversion amplification through dielectric superlensing modulation. *Nat. Commun.* **2019,** *10*, 9.
26. Liu, Q. Y.; Liu, H. C.; Li, D. Y.; Qiao, W.; Chen, G. Y.; Agren, H., Microlens array enhanced upconversion luminescence at low excitation irradiance. *Nanoscale* **2019,** *11* (29), 14070-14078.
27. He, J. J.; Zheng, W.; Ligmajer, F. L.; Chan, C. F.; Bao, Z. Y.; Wong, K. L.; Chen, X. Y.; Hao, J. H.; Dai, J. Y.; Yu, S. F.; Lei, D. Y., Plasmonic enhancement and polarization dependence of nonlinear upconversion emissions from single gold nanorod@SiO2@CaF2:Yb3+,Er3+ hybrid core-shell-satellite nanostructures. *Light-Sci. Appl.* **2017,** *6*, 11.
28. Park, W.; Lu, D. W.; Ahn, S. M., Plasmon enhancement of luminescence upconversion. *Chemical Society Reviews* **2015,** *44* (10), 2940-2962.
29. Sun, Q. C.; Mundoor, H.; Ribot, J. C.; Singh, V.; Smalyukh, II; Nagpal, P., Plasmon-Enhanced Energy Transfer for Improved Upconversion of Infrared Radiation in Doped-Lanthanide Nanocrystals. *Nano Lett.* **2014,** *14* (1), 101-106.
30. Ge, W.; Zhang, X. R.; Liu, M.; Lei, Z. W.; Knize, R. J.; Lu, Y. L., Distance Dependence of Gold-Enhanced Upconversion luminescence in Au/SiO2/Y2O3:Yb3+, Er3+ Nanoparticles. *Theranostics* **2013,** *3* (4), 282-288.
31. Liu, X.; Lei, D. Y., Simultaneous excitation and emission enhancements in upconversion luminescence using plasmonic double-resonant gold nanorods. *Sci Rep* **2015,** *5*, 12.
32. Das, A.; Mao, C. C.; Cho, S.; Kim, K.; Park, W., Over 1000-fold enhancement of upconversion luminescence using water-dispersible metal-insulator-metal nanostructures. *Nat. Commun.* **2018,** *9*, 11.
33. Su, X.; Sun, X. Q.; Wu, S. L.; Zhang, S. F., Manipulating the emission intensity and lifetime of NaYF4:Yb3+,Er3+ simultaneously by embedding it into CdS photonic crystals. *Nanoscale* **2017,** *9* (22), 7666-7673.
34. Shi, Y. H.; Zhang, F. Q.; Xu, J.; Zhou, K.; Chen, C.; Cheng, J.; Li, P., Upconversion fluorescence enhancement of NaYF4:Yb/Re nanoparticles by coupling with SiO2 opal photonic crystals. *J. Mater. Sci.* **2019,** *54* (11), 8461-8471.

35. Gong, C. S.; Liu, W.; He, N.; Dong, H. G.; Jin, Y.; He, S. L., Upconversion enhancement by a dual-resonance all-dielectric metasurface. *Nanoscale* **2019,** *11* (4), 1856-1862.
36. Zhang, J. Y.; Pick, T. E.; Gargas, D.; Dhuey, S.; Chan, E. M.; Wu, Y.; Liang, X. G.; Schuck, P. J.; Olynick, D. L.; Helms, B. A.; Cabrini, S., Probe field enhancement in photonic crystals by upconversion nanoparticles. *J. Vac. Sci. Technol. B* **2011,** *29* (6), 5.
37. Wang, H.; Yin, Z.; Xu, W.; Zhou, D. L.; Cui, S. B.; Chen, X.; Cui, H. N.; Song, H. W., Remarkable enhancement of upconversion luminescence on 2-D anodic aluminum oxide photonic crystals. *Nanoscale* **2016,** *8* (19), 10004-10009.
38. Mao, C. C.; Min, K.; Bae, K.; Cho, S.; Xu, T.; Jeon, H.; Park, W., Enhanced Upconversion Luminescence by Two-Dimensional Photonic Crystal Structure. *ACS Photonics* **2019,** *6* (8), 1882-1888.
39. Liao, J. Y.; Yang, Z. W.; Lai, S. F.; Shao, B.; Li, J.; Qiu, J. B.; Song, Z. G.; Yang, Y., Upconversion Emission Enhancement of NaYF4:Yb,Er Nanoparticles by Coupling Silver Nanoparticle Plasmons and Photonic Crystal Effects. *J. Phys. Chem. C* **2014,** *118* (31), 17992-17999.
40. Wu, D. X.; Rajput, N. S.; Luo, X. C., Nanoimprint Lithography - the Past, the Present and the Future. *Curr. Nanosci.* **2016,** *12* (6), 712-724.
41. Kooy, N.; Mohamed, K.; Pin, L. T.; Guan, O. S., A review of roll-to-roll nanoimprint lithography. *Nanoscale Res. Lett.* **2014,** *9*, 13.
42. Ahn, S. H.; Guo, L. J., Large-Area Roll-to-Roll and Roll-to-Plate Nanoimprint Lithography: A Step toward High-Throughput Application of Continuous Nanoimprinting. *ACS Nano* **2009,** *3* (8), 2304-2310.
43. Becker, C.; Wyss, P.; Eisenhauer, D.; Probst, J.; Preidel, V.; Hammerschmidt, M.; Burger, S., 5 x 5 cm(2) silicon photonic crystal slabs on glass and plastic foil exhibiting broadband absorption and high-intensity near-fields. *Sci Rep* **2014,** *4*, 7.
44. Radunz, S.; Schavkan, A.; Wahl, S.; Würth, C.; Tschiche, H. R.; Krurnrey, M.; Resch-Genger, U., Evolution of Size and Optical Properties of Upconverting Nanoparticles during High-Temperature Synthesis. *J. Phys. Chem. C* **2018,** *122* (50), 28958-28967.
45. Ondic, L.; Varga, M.; Hruska, K.; Fait, J.; Kapusta, P., Enhanced Extraction of Silicon-Vacancy Centers Light Emission Using Bottom-Up Engineered Polycrystalline Diamond Photonic Crystal Slabs. *ACS Nano* **2017,** *11* (3), 2972-2981.
46. Ahiboz, D.; Manley, P.; Becker, C., Adjustable large-area dielectric metasurfaces for near-normal oblique incident excitation. *OSA Continuum* **2020,** *3* (4), 971-981.
47. Berry, M. T.; May, P. S., Disputed Mechanism for NIR-to-Red Upconversion Luminescence in NaYF4:Yb3+,Er3+. *Journal of Physical Chemistry A* **2015,** *119* (38), 9805-9811.
48. Arppe, R.; Hyppanen, I.; Perala, N.; Peltomaa, R.; Kaiser, M.; Wurth, C.; Christ, S.; Resch-Genger, U.; Schaferling, M.; Soukka, T., Quenching of the upconversion luminescence of NaYF4:Yb3+,Er3+ and NaYF4:Yb3+,Tm3+ nanophosphors by water: the role of the sensitizer Yb3+ in non-radiative relaxation. *Nanoscale* **2015,** *7* (27), 11746-11757.
49. Lee, J.; Zhen, B.; Chua, S. L.; Qiu, W. J.; Joannopoulos, J. D.; Soljacic, M.; Shapira, O., Observation and Differentiation of Unique High-Q Optical Resonances Near Zero Wave Vector in Macroscopic Photonic Crystal Slabs. *Phys. Rev. Lett.* **2012,** *109* (6), 5.
50. Kupriianov, A. S.; Xu, Y.; Sayanskiy, A.; Dmitriev, V.; Kivshar, Y. S.; Tuz, V. R., Metasurface Engineering through Bound States in the Continuum. *Phys. Rev. Appl.* **2019,** *12* (1), 8.
51. Wiesholler, L. M.; Frenzel, F.; Grauel, B.; Würth, C.; Resch-Genger, U.; Hirsch, T., Yb,Nd,Er-doped upconversion nanoparticles: 980 nm versus 808 nm excitation. *Nanoscale* **2019,** *11* (28), 13440-13449.
52. Gao, D. L.; Zhang, X. Y.; Chong, B.; Xiao, G. Q.; Tian, D. P., Simultaneous spectra and dynamics processes tuning of a single upconversion microtube through Yb3+ doping concentration and excitation power. *Phys. Chem. Chem. Phys.* **2017,** *19* (6), 4288-4296.
53. Shen, B.; Cheng, S. M.; Gu, Y. Y.; Ni, D. R.; Gao, Y. L.; Su, Q. Q.; Feng, W.; Li, F. Y., Revisiting the optimized doping ratio in core/shell nanostructured upconversion particles. *Nanoscale* **2017,** *9* (5), 1964-1971.
54. Tian, B. N.; Fernandez-Bravo, A.; Najafiaghdam, H.; Torquato, N. A.; Altoe, M. V. P.; Teitelboim, A.; Tajon, C. A.; Tian, Y.; Borys, N. J.; Barnard, E. S.; Anwar, M.; Chan, E. M.; Schuck, P.

J.; Cohen, B. E., Low irradiance multiphoton imaging with alloyed lanthanide nanocrystals. *Nat. Commun.* **2018,** *9*, 8.